

X-ray Spectral Variability of TeV Blazars during Rapid Flares

Yongquan Xue¹, Feng Yuan², and Wei Cui¹

Department of Physics, Purdue University, West Lafayette, IN 47907

ABSTRACT

The spectral energy distribution (SED) of TeV blazars peaks both at keV and TeV energies. The X-ray emission is generally believed to originate in the synchrotron emission from relativistic electrons (and positrons) in the jet of these sources, while the origin of the gamma-ray emission is still being debated. We report results from a systematic study of X-ray spectral variability of Mrk 421 and Mrk 501 during individual flares that last for several days, making use of some of the high-quality data that have recently become available. The X-ray spectra of the two sources fall on the opposite sides of the synchrotron peak of their respective SEDs, so they together may offer additional insights into the physical origin of X-ray variability. We modeled each of the time-resolved X-ray spectra over a *single* flare by adopting a homogeneous spatial distribution and an instantaneous power-law spectral distribution for the emitting particles. We focused on the variation of four key parameters: particle spectral index, maximum Lorentz factor, energy density, and magnetic field. While there is considerable degeneracy in the fits, we show that, in order to account for the X-ray spectral variability observed in Mrk 421, at least three of the parameters are required to vary in most cases, with the spectral index being one of them. The observations of Mrk 501 support the conclusion, although the quality of the data is not as good. We discuss the implications of the results.

Subject headings: BL Lacertae objects: individual (Markarian 421 and Markarian 501) — galaxies: active — radiation mechanisms: non-thermal — X-rays: galaxies

¹Email: xuey@physics.purdue.edu; cui@physics.purdue.edu

²Current address: Shanghai Astronomical Observatory, 80 Nandan Road, Shanghai 200030, P.R. China; fyuan@shao.ac.cn

1. Introduction

Blazars are known to be strong gamma-ray emitters. At TeV energies, BL Lac objects are the only type of blazars that have been detected so far. The spectral energy distribution (SED) of these TeV blazars invariably shows two characteristic peaks in the νF_ν representation, with one located at X-ray energies and the other at TeV energies (e.g., Fossati et al. 1998). While the origin of the TeV emission is still not entirely clear, there is a general consensus that the X-ray emission is associated with the synchrotron radiation from highly relativistic electrons (and positrons) in the jet of blazars. Therefore, studying the X-ray properties of TeV blazars may, in a relatively model-independent manner, shed significant light on the properties of the emitting particles as well as of the environment that they are in.

Blazars are highly variable at nearly all wavelengths. The variability is often in the form of discrete flares. Dramatic rapid flares have been observed of TeV blazars at X-ray energies (e.g., Cui 2004), as well as at TeV energies (e.g., Gaidos et al. 1996), with the former almost certainly being associated with the most energetic electrons in the jet. The observed X-ray flares span a wide range of timescales from many months down to less than an hour, and seem to form a well-organized hierarchy with weaker, shorter-duration flares superimposed on a stronger, longer-duration one (Cui 2004), perhaps indicating a scale-invariant physical origin (see also Xue & Cui 2005). The flaring phenomenon could be related to internal shocks in the jet (Rees 1978; Spada et al. 2001), or to the ejection of relativistic plasma into the jet (e.g., Böttcher et al. 1997; Mastichiadis & Kirk 1997), or to reconnection events in a magnetically dominated jet (Lyutikov 2003).

While it is still difficult to pinpoint the exact mechanism at work, it may have become possible to investigate, quantitatively, which physical parameters evolve most strongly during a *single* flare on a timescale of several days, thanks to improvement in the quality of X-ray data in recent years. In this paper, we report results from such an investigation with two TeV blazars, Mrk 421 and Mrk 501, which are among the first sources discovered at TeV energies (Punch et al. 1992; Quinn et al. 1996; Bradbury et al. 1997). The sources were chosen for this work not only because of the availability of high-quality data but also of their diverse behaviors at X-ray energies. In particular, the observed X-ray spectra of the two sources fall on the opposite sides of the synchrotron peak in their respective SEDs. Modeling their spectra together may, therefore, help reveal common threads underlying the flaring phenomenon in TeV blazars.

2. Observational Aspects

2.1. Data

We observed Mrk 421 regularly with *RXTE* in 2003 and 2004, as part of a multiwavelength monitoring campaign (Błażejowski et al. 2005). The source became exceptionally bright in X-rays near the end of the campaign. Figure 1 shows the relevant portion of the (daily-averaged) ASM light curve. A number of distinct flares are present, with the strongest one peaking roughly at about 10 c/s (or 135 mcrab in the ASM band of 1.5–12 keV)! For detailed spectral studies, we used data from the pointed *RXTE* observations taken with the Proportional Counter Array (PCA). The times of these observations are noted in Fig. 1. The PCA detector consists of five nearly identical proportional counter units (PCUs). However, only PCU 0 and PCU 2 were in use throughout the campaign. PCU 0 has lost its front veto layer, so the data from it are prone to contamination by events caused by low-energy electrons entering the detector. For this work, therefore, we chose PCU 2 as our “standard” detector for flux normalization and spectral analysis. We also only used data taken in the *Standard2*-mode, which have a time resolution of 16 seconds and cover the full energy range (nominally 2–60 keV).

We followed Cui (2004) closely in reducing and analyzing the PCA data. Briefly, the data were reduced with *ftools v5.2*. For a given observation, we first filtered data by following the standard procedure for faint sources,¹ which resulted in a list of good time intervals (GTIs). We then simulated background events for the observation by using the latest background model (`pca_bkgd_cmfaintl7_eMv20031123.mdl`) that is appropriate for faint sources. Using the GTIs, we proceeded to make a spectrum for each PCU by using data from only the first xenon layer (which is most accurately calibrated), which limits the spectral coverage to roughly 3–25 keV. Since few counts are detected at higher energies, the impact of the reduced spectral coverage is very minimal. We repeated the steps to derive a corresponding background spectrum for the PCU from the simulated events.

Unlike Mrk 421, Mrk 501 has been fairly quiet in recent years. For this work, we obtained archival *RXTE* data taken during the 1997 outburst of the source. For direct comparisons we treated the data in the exact same manner as in the case of Mrk 421.

¹See the online *RXTE* Cook Book at http://heasarc.gsfc.nasa.gov/docs/xte/recipes/cook_book.html.

2.2. Results

Figure 2 shows the PCA light curves of Mrk 421 and Mrk 501, covering the respective periods of strong flares. The coverage gaps in both cases are mainly caused by the requirement for coordination with ground-based facilities. For this work, we would ideally like to focus on one single flare and follow the spectral evolution of the source through both the rising and decaying periods. We were able to do so in the case of Mrk 421. A large flare was well sampled by the observations, as shown in Fig. 2, and we chose five of the observations for further analyses. As pointed out by Cui (2004), however, it is, strictly speaking, not possible to isolate a flare from the flaring hierarchy. The notion of “single” flares is therefore meaningful only when a timescale is specified. Here, we are specifically interested in flares that last for days. In the case of Mrk 501, no single flare was adequately sampled. We selected representative observations that covered the rising phase of one flare and the decaying phase of a subsequent flare, as also shown in Fig. 2. Note that Mrk 501 was much fainter than Mrk 421.

For each observation, we jointly fitted the PCU spectra in *XSPEC v11.3.1* (Arnaud 1996). An additional multiplicative factor was introduced to take into account any uncalibrated difference in the overall throughput of the PCUs, with reference to PCU 2. Following the usual practice, we added 1% systematic uncertainty to the data. Given the lack of sensitivity of the PCA below about 2 keV, we adopted the Galactic values for the line-of-sight hydrogen column densities (1.38 and $1.8 \times 10^{20} \text{ cm}^{-2}$ for Mrk 421 and Mrk 501, respectively; Dickey & Lockman 1990) and fixed them in the fitting process.

We experimented with three empirical models: power law, broken power law, and power law with an exponential cut-off. The cut-off power law provides best fits to the data for the selected observations of Mrk 421 (as shown in Fig. 3), although fits with the broken power law are also acceptable. For Mrk 501, the broken and cut-off power law models fit the data almost equally well. In both cases, we used the best-fit model to unfold each observed (count) spectrum to derive the corresponding SED for further theoretical modeling. We should note that only the PCU2 data were used to produce the SED, while data from all active PCUs were used to find the best-fit model.

Figure 3 shows representative X-ray SEDs for Mrk 421 and Mrk 501, respectively. Both sources exhibit significant spectral variability during the flares. In general, the spectrum seems to harden toward high fluxes. It is also clear, from the figure, that the measured X-ray SEDs of Mrk 421 and Mrk 501 lie on the opposite sides of their respective (synchrotron) peaks, which are (mostly) below 2 keV in the former case but above 20 keV in the latter. Therefore, together, the sources should be representative of TeV blazars.

3. Theoretical Aspects

To gain insights into variability of the underlying distribution of electrons, as well as their environment, we proceeded to construct a physical model and to apply the model to the data in a systematic manner.

3.1. Model

We assume that each flare of interest originates in one localized region in the jet and that the electron and magnetic field are distributed homogeneously in the region. We further assume that the energy spectrum of *emitting* electrons is of power-law shape,

$$n(\gamma)d\gamma = N_0\gamma^{-p}d\gamma, \quad \gamma_{\min} \leq \gamma \leq \gamma_{\max}. \quad (1)$$

The total energy density of electrons is then

$$E_{\text{tot}} = N_0 m_e c^2 \frac{\gamma_{\min}^{2-p} - \gamma_{\max}^{2-p}}{p-2}, \quad p \neq 2. \quad (2)$$

For an electron with Lorentz factor of γ , the differential power of its synchrotron radiation is given by

$$\frac{dP(\nu)}{d\nu} = \frac{2\pi\sqrt{3}e^2\nu_L}{c} \left[\frac{\nu}{\nu_c} \int_{\nu/\nu_c}^{\infty} K_{5/3}(t) dt \right] (\text{erg s}^{-1} \text{ Hz}^{-1}), \quad (3)$$

where the Larmor frequency $\nu_L = \frac{1}{2\pi} \frac{eB}{m_e c}$, the critical frequency $\nu_c = \frac{3}{2}\nu_L\gamma^2$, and $K_n(t)$ is the modified Bessel function of the second kind of order n . Assuming that the flaring region is of spherical shape with radius r , the spectrum of the integrated emission (in the jet frame) is

$$F_\nu = \frac{4}{3}\pi r^3 \int_{\gamma_{\min}}^{\gamma_{\max}} n(\gamma) \frac{dP(\nu)}{d\nu} d\gamma. \quad (4)$$

If the Doppler factor of the jet is δ , the observed spectrum is given by

$$F_{\text{obs}}(\nu^{\text{obs}}) = \delta^3 F_\nu(\nu^{\text{obs}}/\delta) \quad (5)$$

It is often taken casually that such an optically-thin synchrotron spectrum is also of power-law shape with a spectral index of $\alpha = (p-1)/2$. This is only true when the portion of the spectrum of interest is far away from the critical frequencies corresponding to either γ_{\min} or γ_{\max} . The issue is of particular relevance to the case of Mrk 421 because its X-ray spectrum

seems to be entirely associated with electrons near γ_{\max} , as shown in Fig. 3. Therefore, care must be taken in the calculation.

There are many parameters in the model. The objective of this work is to systematically investigate the roles of “key” parameters in producing the observed X-ray spectral variability during a major flare. We identified these parameters as: p , γ_{\max} , E_{tot} , and B . We adopted E_{tot} rather than N_0 because (1) it seems obvious that N_0 must vary during a flare, so few insights would be gained; and (2) E_{tot} , though depending on other parameters of interest, is a well-defined physical quantity and provide important information on the energetics of the flaring process. All other parameters were fixed during the fitting process. The size of the emitting region was chosen to be compatible with the observed timescale of the flare, $r = 1 \times 10^{16}$ and 5×10^{15} cm for Mrk 421 and Mrk 501, respectively; the Doppler factor was set at a nominal value for TeV blazars ($\delta = 15$); and the minimum Lorentz factor of the electrons was made sufficiently low ($\gamma_{\min} = 10^4$) such that it does not affect the conclusions reached. For this work, we adopted the luminosity distances of $d = 137$ and 156 Mpc for Mrk 421 ($z = 0.030$) and Mrk 501 ($z = 0.034$), respectively, which were derived with the following cosmological parameters: $H = 65$ km s $^{-1}$ Mpc $^{-1}$, $\Omega_m = 0.3$, and $\Omega_\Lambda = 0.7$.

3.2. Results

For each spectrum shown in Fig. 3, a grid search was carried out to find statistically acceptable solutions. A solution is defined as a combination of p , γ_{\max} , E_{tot} , and B that leads to a fit with reduced χ^2 in the range of $1 \pm \sqrt{2/\nu}$, where ν is the degree of freedom of the fit. Note that a χ^2 distribution can be approximated by a normal distribution with mean of ν and standard deviation of $\sqrt{2\nu}$ when ν is sufficiently large. Here, ν is typically 30–40. The ranges of the parameters covered in the search are: p in 1.00–4.00, B in 10^{-3} – 10^2 G, γ_{\max} in 10^5 – 10^{11} , and E_{tot} in 10^8 – 10^{15} cm $^{-3}$. The step used is linear for p , with $\Delta p = 0.01$, but logarithmic for B , γ_{\max} , and E_{tot} , with 50 and 25 points per decade for Mrk 421 and Mrk 501, respectively.

Table 1 summarizes the results for Mrk 421 and Mrk 501 separately. The ranges shown indicate the portion of the parameter space where solutions are found. It is quite clear that p is quite well constrained in both cases. For illustration, Fig. 4 shows the distributions of p for Mrk 421. The p distribution is nicely peaked. The most probable values of p are also shown in Table 1 for both sources. The results seems to indicate that the electron spectrum tends to harden toward the peak of a flare. There is a substantial amount of degeneracy among the other three parameters: γ_{\max} is fairly well constrained in Mrk 421 but not at all in Mrk 501 (presumably due to poorer data quality); B is poorly constrained in both cases;

and E_{tot} is not constrained at all. The distributions of these parameters are fairly flat with no dominant peaks. The best fits are shown in Fig. 3.

To break the degeneracy, we proceeded to examine specialized cases, in which a subset of the parameters are fixed at some “typical” values, as seen from modeling broadband SEDs of the sources. It became immediately clear that, to account for the observed X-ray spectral variability of Mrk 421, p *cannot* be fixed. This is not the case for Mrk 501, presumably due to the poorer statistics again. Taking the view that the same processes are operating in both sources, we allowed p to vary in all subsequent analyses.

We first experimented with fixing one of the remaining parameters, B , γ_{max} , and E_{tot} . We found acceptable fits to *all* of the spectra in all cases. As examples, Table 2 and Table 3 show the results obtained with $B = 0.10, 0.83$ G and $\gamma_{\text{max}} = 5.0 \times 10^5, 5.2 \times 10^6$ for Mrk 421 and Mrk 501, respectively (see, e.g., Błażejowski et al 2005 and Pian et al. 1998). The free parameters are now much more constrained. We then proceeded to investigate whether we could fix two of the parameters and still obtain solutions. We found that it was not possible to account for the observed spectral variability in Mrk 421, except for the case in which B and γ_{max} were fixed, which confirms that the synchrotron peak of the SED ($\propto \gamma_{\text{max}}^2 B$) did not vary too much during the flare. As for Mrk 501, the data are much less constraining; we were still able to find satisfactory fits to the spectra. For completeness, we also examined the possibility of fixing all three parameters. In this case, we failed to obtain acceptable fits to *all* of the spectra for either source.

It is often assumed that the ratio of the energy of the radiating particles to that of the magnetic field remains constant, in theoretical studies of gamma ray bursts and blazars. To check if the assumption can be accommodated by the data, we looked at cases in which E_{tot}/B^2 remains constant. For both sources, acceptable solutions were found. As an example, we show in Table 4 those solutions selected from the full set (as shown in Table 1) that have E_{tot}/B^2 fixed at some fiducial values. In this case, the other parameters are even more constrained, although it is not possible to know the exact value of the ratio *a priori*.

4. Discussion

We have obtained time-resolved X-ray spectra of Mrk 421 during the rise and fall of a prominent X-ray flare, as well as of Mrk 501 during two consecutive flares (on a timescale of a few days) for comparison. In general, the X-ray spectrum steepens as the flux decreases (see Fig. 3), as was seen previously in X-ray selected BL Lac objects in general (Giommi et al. 1990). For Mrk 421, the synchrotron peak is clearly below the low-energy sensitivity

threshold of the PCA detector (~ 2 keV), judging from the shape of the SEDs, except for one case (“ t_3 ” in Fig. 3) in which the peak appears to have moved into the PCA passing band. A shift in the synchrotron peak with flux has been seen in Mrk 501 previously (Pian et al. 1998; Sambruna et al. 2000). In our case, the synchrotron peak of Mrk 501 is clearly above the spectral range of the data shown in Fig. 3 (but not necessarily above that of the PCA), which is known (e.g., Pian et al. 1998; Catanese et al. 1997; Lamer & Wagner 1998), and is also why we selected it for comparison with Mrk 421 in the first place. Because of that, our SED modeling suffers from serious degeneracy between B and γ_{\max} . For instance, the unusually-high values allowed for γ_{\max} or unusually-low values for B is the consequence of such uncertainty.

To cast light on the origin of the observed X-ray spectral variability of both Mrk 421 and Mrk 501, we took an approach to model *instantaneous* properties of the sources throughout the flares. In other words, we were *not* concerned with the steady-state properties. For simplicity, we assumed that the emitting electrons always follow a power-law spectral distribution, which may or may not be the case in reality, after heating and cooling processes are properly taken into account. Moreover, we assumed that the spatial distribution of the electrons is homogeneous during a flare. Even with such an idealistic approach, the model still contains too many parameters to de-couple completely. We narrowed our focus onto the evolution of four key parameters: p , γ_{\max} , E_{tot} , and B , with other parameters fixed at nominal values derived from variability timescales and broadband SEDs (in particular, the TeV gamma-ray properties). In spite of serious degeneracy in the solutions, we are able to reach a few conclusions that we think are robust.

As expected, the high-quality data of Mrk 421 have provided the most severe constraints on the model. To account for the observed spectral variability of the source, we found that the electron spectral index (p) must vary. There appears to be a general trend of decreasing p toward high fluxes. The only exception seen (t_1 in Fig. 4) is probably due to “contamination” by a previous flare (see Fig. 2). Of course, it could also be associated with local variability *within* the flare of interest. Again, there may always be smaller flares superimposed on it (Cui 2004). The change in p alone is, however, not sufficient for explaining the observed X-ray spectral variability. At least two of the three remaining parameters must also vary, in all but one combinations. The lone exception is that acceptable solutions do exist even when B and γ_{\max} are both fixed. This is an indication that the synchrotron peak did not vary too much during the flare. Even when all four parameters are allowed to vary, both p and γ_{\max} are reasonably well constrained (see Table 1). If we set B or γ_{\max} at typical values from modeling the broadband SED, as well as time variability, in the context of the synchrotron self-Compton scenario, the other parameters are much more constrained and their values are also quite typical (see Tables 2 and 3).

The quality of data is not nearly as good for Mrk 501 as for Mrk 421. However, we feel that it is a worthwhile exercise to see whether the same model can also be applied to a different TeV blazar, like Mrk 501 whose observed X-ray spectrum is almost entirely below the synchrotron peak. We followed precisely the same procedures in modeling the X-ray spectra of Mrk 501 as Mrk 421. From Tables 1, 2, and 3, it is clear that the model parameters are poorly constrained in this case. One interesting (and solid) result is that the electron spectrum is much harder for Mrk 501 than for Mrk 421, even after taking into account the large uncertainties. Moreover, the electron spectrum hardens toward high fluxes during the rising phase of the first flare, although the trend is not as clear during the decaying phase of the second flare, perhaps due to the presence of more complicated local variability (see Fig. 2). Because the synchrotron peak is beyond the energy range covered by the data in this case, B and γ_{\max} are hardly constrained.

We should stress that it is not our goal to exhaustively explore the entire parameter space of the model. The scope of our investigation is limited only to a few selected parameters, which could affect the conclusions. First of all, although the effects of some of the parameters not selected (e.g., the size of the emitting region) can be absorbed into E_{tot} , those of others may still contribute to the observed X-ray spectral variability. For instance, the Doppler factor of the jet might not remain constant during a flare and thus lead to not only variable Doppler boosting of the source intensity (which only affects the overall normalization) but also variable Doppler shift of the photon energy (see Eq. 5). We should note, however, that we also ran a case for Mrk 421 where the size of the emitting region and the Doppler factor were fixed at very different values ($R = 10^{15}$ cm and $\delta = 50$). Although the exact values of the best-fit parameters are different, our conclusions remain the same. Second, the homogeneous electron distribution considered here may be a gross over-simplification of the reality. Multiple electron populations may be present, with different properties and environments, and all may contribute to the X-ray emission. However, in our view, it seems more likely that a single rapid flare is associated with one electron population, which is why we tried to focus on specific flares. The most important conclusion of this study is that the observed X-ray spectral variability of TeV blazars is likely caused by a combination of spectral variation of the radiating electrons and changes in the environment (e.g., B). This is hardly surprising because it seems unlikely that, in reality, the triggering of a flare involves changes only in one of the parameters. Moreover, our results show that the spectral index (p) of the particle distribution must vary during a flare, together with the overall normalization (N_0).

This work was supported in part by NASA Grants NAG5-13736 and NNG04GP86G. It has made use of data obtained through the High Energy Astrophysics Science Archive

Research Center Online Service, provided by the NASA/Goddard Space Flight Center, and through the NASA/IPAC Extragalactic Database, which is operated by the Jet Propulsion Laboratory, California Institute of Technology.

Table 1: Spectral Solutions: Full Set

Observation (Data Set)	MJD	p mpv(min,max) ^b	B (Gauss) (min,max)	γ_{\max} (min,max)	E_{tot} (cm ⁻³) ^a (min,max)
421 t_1	53114.25	3.16(3.04,3.27)	(0.002,3.98)	($1.9 \times 10^5, 8.3 \times 10^6$)	($10^8, 10^{15}$)
421 t_2	53115.31	3.45(3.20,3.64)	(0.003,5.25)	($1.5 \times 10^5, 6.0 \times 10^6$)	($10^8, 10^{15}$)
421 t_3	53116.30	2.76(2.54,2.93)	(0.002,4.57)	($1.7 \times 10^5, 9.5 \times 10^6$)	($10^8, 10^{15}$)
421 t_4	53118.24	3.39(3.13,3.57)	(0.003,5.50)	($1.4 \times 10^5, 6.0 \times 10^6$)	($10^8, 10^{15}$)
421 t_5	53119.25	3.87(3.26,3.95)	(0.002,4.37)	($1.7 \times 10^5, 1.0 \times 10^{11}$)	($10^8, 10^{15}$)
501 T_1	50553.37	2.60(1.77,2.73)	(0.002,75.9)	($1.7 \times 10^5, 1.0 \times 10^{11}$)	($10^8, 10^{15}$)
501 T_2	50554.17	2.28(1.35,2.46)	(0.002,100.)	($1.7 \times 10^5, 1.0 \times 10^{11}$)	($10^8, 10^{15}$)
501 T_3	50554.44	2.13(1.04,2.45)	(0.002,100.)	($1.6 \times 10^5, 1.0 \times 10^{11}$)	($10^8, 10^{15}$)
501 T_4	50580.36	2.56(1.76,2.71)	(0.002,91.2)	($1.7 \times 10^5, 1.0 \times 10^{11}$)	($10^8, 10^{15}$)
501 T_5	50581.19	2.30(1.39,2.71)	(0.002,83.2)	($1.6 \times 10^5, 1.0 \times 10^{11}$)	($10^8, 10^{15}$)
501 T_6	50581.36	2.07(1.57,2.37)	(0.002,6.31)	($1.9 \times 10^5, 1.3 \times 10^7$)	($10^8, 10^{15}$)
501 T_7	50582.36	2.63(1.32,2.72)	(0.002,75.9)	($1.6 \times 10^5, 1.0 \times 10^{11}$)	($10^8, 10^{15}$)

^a E_{tot} has been scaled by the electron rest energy

^b mpv: most probable value

Table 2: Spectral Solutions: Subset with Fixed B

Observation (Data Set)	MJD	p mpv(min,max)	B (Gauss) (fixed)	γ_{\max} (min,max)	E_{tot} (cm ⁻³) (min,max)
421 t_1	53114.25	3.11(3.05,3.23)	0.10	($1.1 \times 10^6, 1.3 \times 10^6$)	($2.5 \times 10^{11}, 3.5 \times 10^{11}$)
421 t_2	53115.31	3.48(3.22,3.62)	0.10	($1.0 \times 10^6, 1.3 \times 10^6$)	($4.6 \times 10^{11}, 1.1 \times 10^{12}$)
421 t_3	53116.30	2.75(2.62,2.89)	0.10	($1.1 \times 10^6, 1.3 \times 10^6$)	($2.3 \times 10^{11}, 3.2 \times 10^{11}$)
421 t_4	53118.24	3.34(3.14,3.56)	0.10	($1.0 \times 10^6, 1.3 \times 10^6$)	($4.6 \times 10^{11}, 1.1 \times 10^{12}$)
421 t_5	53119.25	3.88(3.30,3.95)	0.10	($9.5 \times 10^5, 1.0 \times 10^{11}$)	($2.5 \times 10^{11}, 1.2 \times 10^{12}$)
501 T_1	50553.37	2.60(1.91,2.71)	0.83	($4.8 \times 10^5, 1.0 \times 10^{11}$)	($4.8 \times 10^9, 2.3 \times 10^{12}$)
501 T_2	50554.17	2.28(1.75,2.34)	0.83	($6.3 \times 10^5, 1.0 \times 10^{11}$)	($8.3 \times 10^9, 7.6 \times 10^{13}$)
501 T_3	50554.44	1.97(1.04,2.31)	0.83	($4.4 \times 10^5, 2.5 \times 10^6$)	($6.9 \times 10^9, 2.3 \times 10^{10}$)
501 T_4	50580.36	2.56(1.94,2.63)	0.83	($5.2 \times 10^5, 1.0 \times 10^{11}$)	($6.3 \times 10^9, 2.8 \times 10^{12}$)
501 T_5	50581.19	2.42(1.62,2.63)	0.83	($4.4 \times 10^5, 5.8 \times 10^9$)	($5.2 \times 10^9, 2.8 \times 10^{11}$)
501 T_6	50581.36	2.04(1.78,2.31)	0.83	($4.8 \times 10^5, 6.9 \times 10^5$)	($5.2 \times 10^9, 6.9 \times 10^9$)
501 T_7	50582.36	2.63(1.38,2.67)	0.83	($3.6 \times 10^5, 9.1 \times 10^{10}$)	($3.6 \times 10^9, 6.3 \times 10^{11}$)

Table 3: Spectral Solutions: Subset with Fixed γ_{\max}

Observation (Data Set)	MJD	p mpv(min,max)	B (Gauss) (min,max)	γ_{\max} (fixed)	E_{tot} (cm^{-3}) (min,max)
421 t_1	53114.25	3.09(3.07,3.12)	(0.52,0.58)	5.0×10^5	$(6.6 \times 10^9, 7.6 \times 10^9)$
421 t_2	53115.31	3.45(3.23,3.60)	(0.40,0.69)	5.0×10^5	$(1.1 \times 10^{10}, 2.5 \times 10^{10})$
421 t_3	53116.30	2.76(2.59,2.89)	(0.50,0.76)	5.0×10^5	$(4.6 \times 10^9, 8.3 \times 10^9)$
421 t_4	53118.24	3.39(3.13,3.56)	(0.40,0.69)	5.0×10^5	$(1.3 \times 10^{10}, 2.4 \times 10^{10})$
421 t_5	53119.25	3.80(3.29,3.92)	(0.36,4.17)	5.0×10^5	$(1.0 \times 10^8, 1.6 \times 10^{10})$
501 T_1	50553.37	2.58(1.88,2.70)	(0.01,15.8)	5.2×10^6	$(1.0 \times 10^8, 8.3 \times 10^{13})$
501 T_2	50554.17	2.26(1.35,2.34)	(0.01,30.2)	5.2×10^6	$(1.0 \times 10^8, 1.0 \times 10^{14})$
501 T_3	50554.44	1.98(1.04,2.32)	(0.01,0.25)	5.2×10^6	$(2.8 \times 10^{11}, 1.4 \times 10^{14})$
501 T_4	50580.36	2.55(1.76,2.62)	(0.01,17.4)	5.2×10^6	$(1.0 \times 10^8, 1.0 \times 10^{14})$
501 T_5	50581.19	2.29(1.60,2.58)	(0.01,0.05)	5.2×10^6	$(2.8 \times 10^{12}, 1.3 \times 10^{14})$
501 T_6	50581.36	2.04(1.58,2.36)	(0.01,0.02)	5.2×10^6	$(2.1 \times 10^{13}, 1.2 \times 10^{14})$
501 T_7	50582.36	2.60(1.32,2.66)	(0.01,13.2)	5.2×10^6	$(1.0 \times 10^8, 1.6 \times 10^{14})$

Table 4: Spectral Solutions: Subset with Fixed E_{tot}/B^2

Observation (Data Set)	MJD	p mpv(min,max)	B (Gauss) (min,max)	γ_{\max} (min,max)	E_{tot} (cm^{-3}) (min,max)
421 t_1	53114.25	3.11(3.05,3.16)	(0.10,0.11)	$(1.1 \times 10^6, 1.2 \times 10^6)$	$(2.5 \times 10^{11}, 2.8 \times 10^{11})$
421 t_2	53115.31	3.49(3.31,3.59)	(0.12,0.14)	$(9.5 \times 10^5, 1.1 \times 10^6)$	$(3.6 \times 10^{11}, 4.8 \times 10^{11})$
421 t_3	53116.30	2.78(2.70,2.86)	(0.10,0.11)	$(1.2 \times 10^6, 1.3 \times 10^6)$	$(2.5 \times 10^{11}, 2.8 \times 10^{11})$
421 t_4	53118.24	3.36(3.23,3.52)	(0.12,0.14)	$(9.5 \times 10^5, 1.0 \times 10^6)$	$(3.6 \times 10^{11}, 4.8 \times 10^{11})$
421 t_5	53119.25	3.83(3.30,3.91)	(0.10,0.14)	$(9.5 \times 10^5, 1.0 \times 10^{11})$	$(2.5 \times 10^{11}, 4.8 \times 10^{11})$
501 T_1	50553.37	2.60(2.27,2.71)	(0.28,1.20)	$(1.1 \times 10^6, 1.0 \times 10^{11})$	$(5.8 \times 10^{10}, 1.1 \times 10^{12})$
501 T_2	50554.17	2.28(2.15,2.34)	(0.33,3.31)	$(1.9 \times 10^6, 1.0 \times 10^{11})$	$(8.3 \times 10^{10}, 8.3 \times 10^{12})$
501 T_3	50554.44	1.85(1.70,2.27)	(0.30,0.36)	$(1.0 \times 10^6, 2.8 \times 10^6)$	$(6.9 \times 10^{10}, 1.0 \times 10^{11})$
501 T_4	50580.36	2.56(1.92,2.62)	(0.28,1.20)	$(9.1 \times 10^5, 1.0 \times 10^{11})$	$(5.8 \times 10^{10}, 1.1 \times 10^{12})$
501 T_5	50581.19	2.46(2.05,2.60)	(0.28,0.58)	$(9.1 \times 10^5, 5.2 \times 10^8)$	$(5.8 \times 10^{10}, 2.5 \times 10^{11})$
501 T_6	50581.36	2.18(2.15,2.22)	(0.28,0.28)	$(1.0 \times 10^6, 1.0 \times 10^6)$	$(5.8 \times 10^{10}, 5.8 \times 10^{10})$
501 T_7	50582.36	2.63(1.82,2.66)	(0.25,0.76)	$(8.3 \times 10^5, 3.3 \times 10^{10})$	$(4.8 \times 10^{10}, 4.4 \times 10^{11})$

REFERENCES

- Arnaud, K. A. 1996, ASPC, 101, 17
- Błażejowski, M. et al. 2005, ApJ, 630, 130
- Böttcher, M., et al. 1997, A&A, 324, 395
- Bradbury, S. et al. 1997, A&A, 320, L5
- Catanese, M. et al. 1997, ApJ, 487, L143
- Cui, W. 2004, ApJ, 605, 662
- Dickey, J. M., & Lockman, F. J. 1990, ARA&A, 28, 215
- Fossati, G. et al. 1998, MNRAS, 299, 433
- Gaidos, J., et al. 1996, Nature, 383, 319
- Giommi, P. et al. 1990, ApJ, 356, 432
- Lamer, G., & Wagner, S. J. 1998, A&A, 331, L13
- Lyutikov, M. 2003, New Astr. Rev. 47, 513
- Mastichiadis, A., & Kirk, J. G. 1997, A&A, 320, 19
- Pian, E. et al. 1998, ApJ, 492, L17
- Punch, M., et al. 1992, Nature, 358, 477
- Quinn, J. et al. 1996, ApJ, 456, L83
- Rees, M. J. 1978, MNRAS, 184, P61
- Sambruna, R. et al. 2000, 538, 127
- Spada, M., et al. 2001, MNRAS, 325, 1559
- Xue, Y. Q. & Cui, W. 2005, ApJ, 622, 160

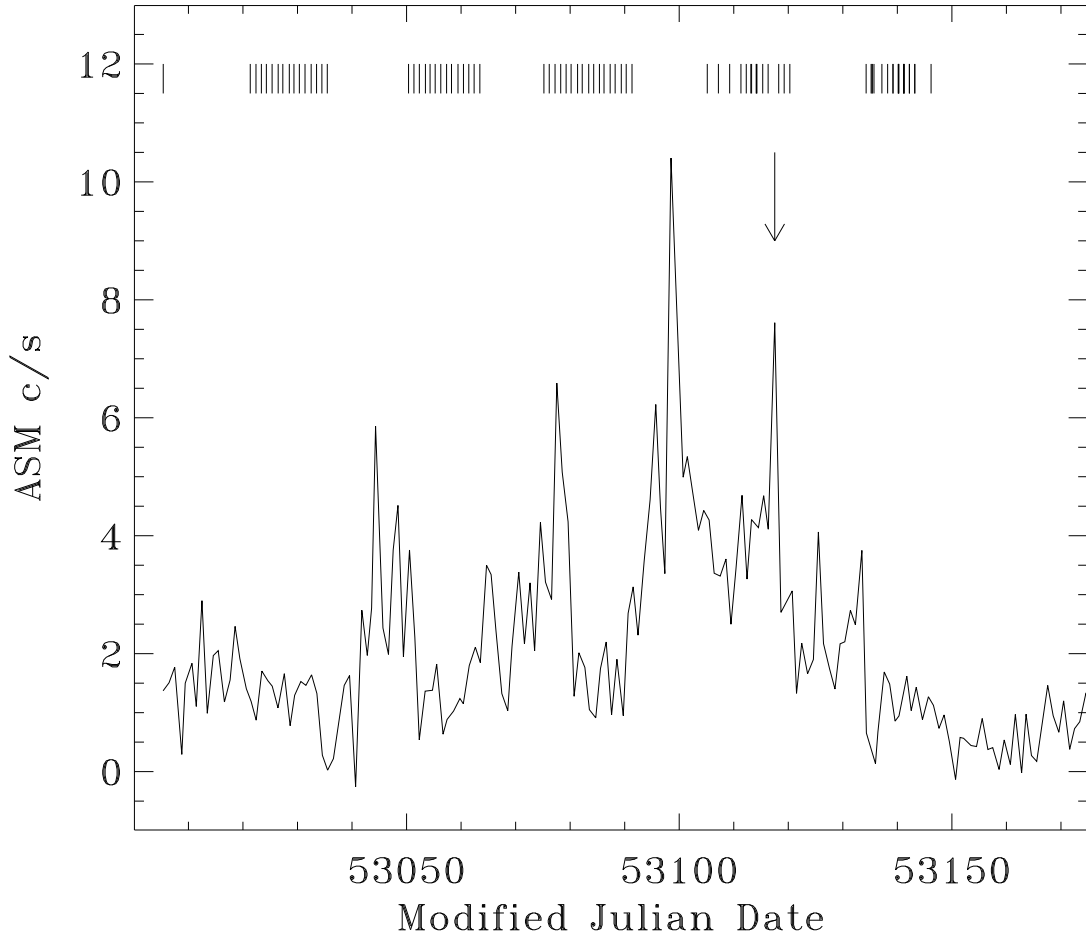


Fig. 1.— Daily-binned ASM light curve of Mrk 421 in 2004. Each data point represents a weighted average of raw count rates in the summed band (1.5–12 keV) over 1 day. For clarity, the error bars are not shown. The times of the pointed PCA/*RXTE* observations are indicated with vertical lines at the top. The arrow points to a flare that was very well covered by the PCA observations. For reference, the Crab Nebula produces about 75 c/s.

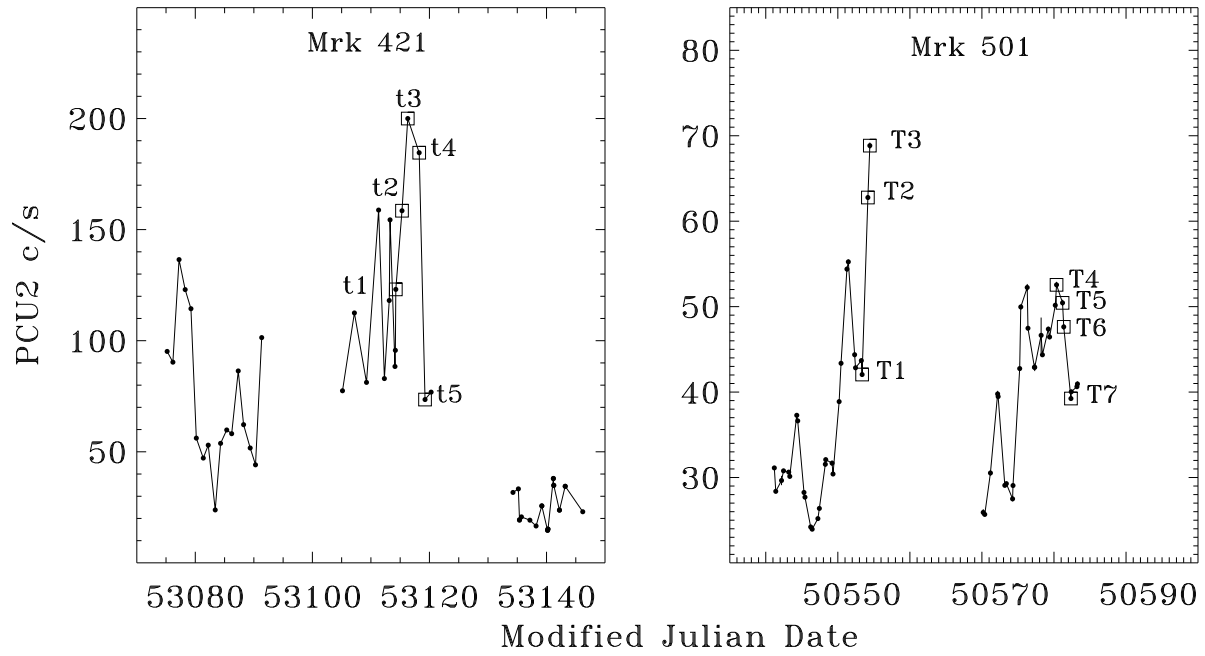


Fig. 2.— PCA light curves of Mrk 421 in 2004 (*left*) and Mrk 501 in 1997 (*right*). The results were derived from the PCU 2 data alone. The count rates were computed in the 2–60 keV band. For reference, the Crab Nebula produces about 2700 c/s/PCU. The observations selected for subsequent analyses are marked. Note the presence of coverage gaps.

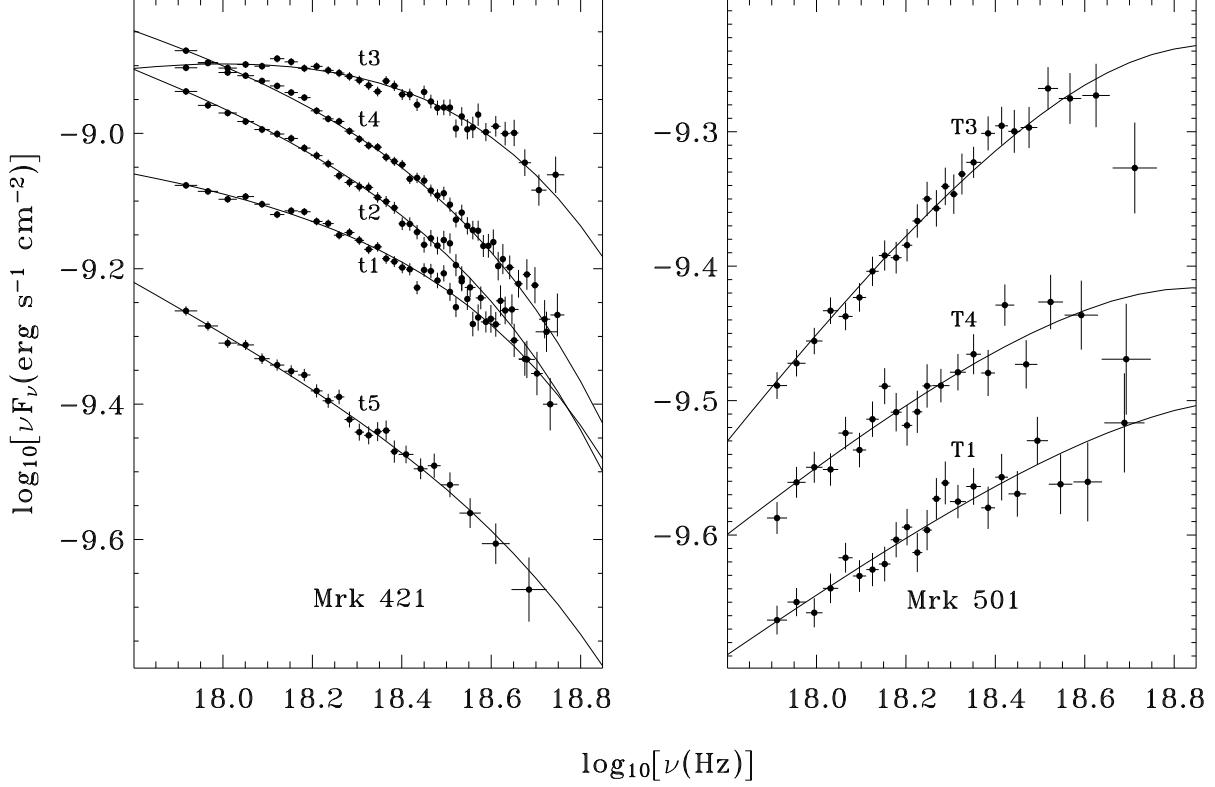


Fig. 3.— Representative X-ray spectra of Mrk 421 (*left*) and Mrk 501 (*right*). The solid lines show the best-fit models. The parameters are: for Mrk 421, (*t1*: $p = 3.16$, $B = 0.22$, $\gamma_{\max} = 8.2 \times 10^5$, $E_{\text{tot}} = 1.05 \times 10^{11}$), (*t2*: $p = 3.45$, $B = 0.25$, $\gamma_{\max} = 7.1 \times 10^5$, $E_{\text{tot}} = 1.75 \times 10^{11}$), (*t3*: $p = 2.72$, $B = 0.21$, $\gamma_{\max} = 8.3 \times 10^5$, $E_{\text{tot}} = 1.05 \times 10^{11}$), (*t4*: $p = 3.38$, $B = 0.31$, $\gamma_{\max} = 6.3 \times 10^5$, $E_{\text{tot}} = 1.1 \times 10^{11}$), (*t5*: $p = 3.71$, $B = 0.29$, $\gamma_{\max} = 7.9 \times 10^5$, $E_{\text{tot}} = 0.95 \times 10^{11}$); for Mrk 501, (*T1*: $p = 2.52$, $B = 0.10$, $\gamma_{\max} = 3.1 \times 10^6$, $E_{\text{tot}} = 5.0 \times 10^{11}$), (*T3*: $p = 2.07$, $B = 0.10$, $\gamma_{\max} = 2.2 \times 10^6$, $E_{\text{tot}} = 6.5 \times 10^{11}$), (*T4*: $p = 2.44$, $B = 0.11$, $\gamma_{\max} = 2.4 \times 10^6$, $E_{\text{tot}} = 4.6 \times 10^{11}$).

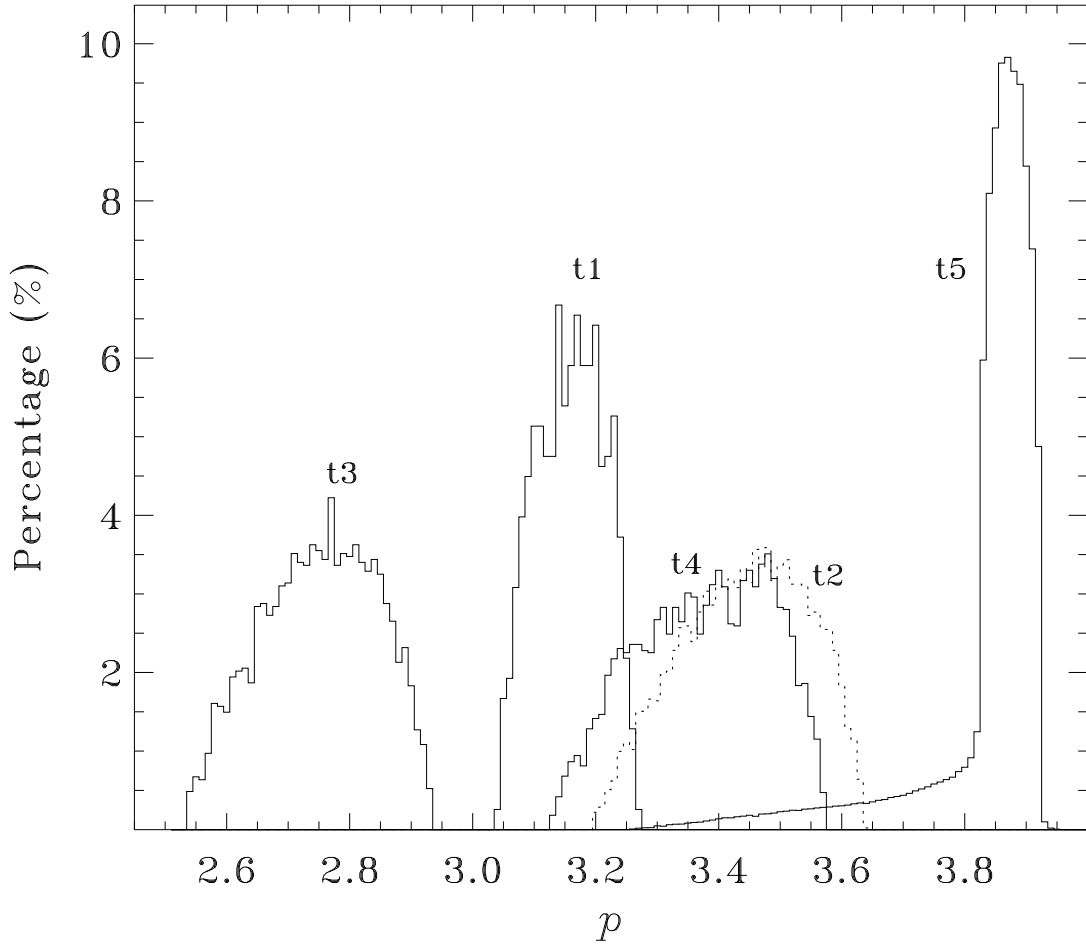


Fig. 4.— Normalized distributions of the electron spectral index for Mrk 421. The results shown were derived for the case in which all key parameters are allowed to vary (see text).